ENGINEERING

Van der Waals engineering of ferromagnetic semiconductor heterostructures for spin and valleytronics

Ding Zhong,[1]* Kyle L. Seyler,[1]* Xiayu Linpeng,[1]* Ran Cheng,[2] Nikhil Sivadas,[2] Bevin Huang,[1] Emma Schmidgall,[1] Takashi Taniguchi,[3] Kenji Watanabe,[3] Michael A. McGuire,[4] Wang Yao,[5] Di Xiao,[2] Kai-Mei C. Fu,[1,6] Xiaodong Xu[1,7]†

The integration of magnetic material with semiconductors has been fertile ground for fundamental science as well as of great practical interest toward the seamless integration of information processing and storage. We create van der Waals heterostructures formed by an ultrathin ferromagnetic semiconductor CrI_3 and a monolayer of WSe_2. We observe unprecedented control of the spin and valley pseudospin in WSe_2, where we detect a large magnetic exchange field of nearly 13 T and rapid switching of the WSe_2 valley splitting and polarization via flipping of the CrI_3 magnetization. The WSe_2 photoluminescence intensity strongly depends on the relative alignment between photoexcited spins in WSe_2 and the CrI_3 magnetization, because of ultrafast spin-dependent charge hopping across the heterostructure interface. The photoluminescence detection of valley pseudospin provides a simple and sensitive method to probe the intriguing domain dynamics in the ultrathin magnet, as well as the rich spin interactions within the heterostructure.

INTRODUCTION

Manipulating exchange interactions in magnetic heterostructures has proven to be an effective way to engineer highly functional materials. For example, control of the interlayer exchange coupling (*1*–*3*) and exchange bias (*4*) has enabled widely used magnetic storage technologies, such as giant magnetoresistance (*2*, *3*) and magnetic tunnel junctions (*5*). Currently, there is intense focus to expand the class of functional materials that can use magnetism via proximity exchange effects. Heterostructures of magnetic material integrated with superconductors (*6*), topological insulators (*7*, *8*), and semiconductors (*9*) have been proposed and investigated. The incorporation of magnetism with semiconductor electronics is particularly enticing for spintronic applications (*10*, *11*). For example, exchange interactions between the ferromagnet spins and semiconductor charge carriers lead to a tunable spin polarization (*12*–*14*). Our work extends this field into new territory by constructing and exploring the exchange interactions in a van der Waals interface between a monolayer WSe_2 semiconductor and an ultrathin ferromagnetic semiconductor CrI_3.

The use of two-dimensional (2D) materials to form magnetic heterostructures has the advantage that the proximity-induced exchange interaction, which is usually considered as a perturbative effect for bulk materials, can fundamentally alter the electronic structure of the 2D material. Theoretical work has predicted strong exchange effects (*15*, *16*) and emergent phenomena (*17*–*21*) in systems that integrate 2D materials with bulk, 3D magnets. Proximity-induced exchange effects have been experimentally demonstrated in graphene/EuS heterostructures (*22*, *23*), and recently, valley-polarized electroluminescence from 2D semiconductors has been achieved (*24*, *25*). In this latter case, the degree of polarization remains modest, and the effect of exchange fields has not been observed. Furthermore, because of the polycrystalline nature and small grain size of the 3D magnets in these devices, external magnetic fields are required to polarize the ferromagnets for any observable magnetic functionality.

Compared to the approach to interfacing 2D materials with 3D magnets, a van der Waals heterostructure has several advantages (*26*–*28*). Lattice mismatch is not an issue, thus minimizing chemical modification and interfacial damage, which is desirable for engineering a clean interface for optimal interactions. Because single crystals are used, the twist angle and stacking order between constituent 2D materials become a potentially powerful control knob, enabling, for instance, the ability to engineer and study magnetic multilayer van der Waals stacks with unique spin textures. The flexibility of the layer stacking process also facilitates the creation of van der Waals heterostructures between layered ferromagnets and a diverse set of other 2D materials, such as graphene, Weyl semimetals (WTe_2), superconductors ($NbSe_2$), and so on.

Here, we report that a van der Waals ferromagnetic heterostructure formed by monolayer WSe_2 and ultrathin CrI_3 enables unprecedented control of spin and valley pseudospin in monolayer WSe_2 while revealing a new platform to study the dynamics of layered magnets. Figure 1A displays the heterostructure architecture, where vertically stacked monolayer WSe_2 and ~10-nm CrI_3 (Fig. 1B) are sandwiched by thin (10 to 20 nm) hexagonal boron nitride (h-BN) flakes to prevent sample degradation (see Materials and Methods). We present results from two devices (12- and 9-nm CrI_3), which show similar behavior, and a top view of device 2 is shown in Fig. 1C. In our design, we use monolayer semiconducting WSe_2 because of its well-established spin and valley pseudospin properties (Fig. 1D, dashed lines), including circularly polarized valley optical selection rules (*29*), spin-valley locking effects (*30*), and valley Zeeman splitting of about 0.22 meV/T (*31*–*34*). CrI_3 (Fig. 1B) is a layered ferromagnetic semiconductor with an optical gap near 1.2 eV (*35*). Bulk CrI_3 crystal exhibits a Curie temperature (T_C) of 61 K, a saturation magnetization of 3.1 Bohr magneton per Cr, and an out-of-plane easy axis (*36*). The last feature is important because the spin quantization axis is also out-of-plane in WSe_2, with opposite orientations in opposite valleys due to the spin-valley locking effect (Fig. 1D). Thus, only perpendicular effective magnetic fields can lift the valley degeneracy.

[1]Department of Physics, University of Washington, Seattle, WA 98195, USA. [2]Department of Physics, Carnegie Mellon University, Pittsburg, PA 15213, USA. [3]National Institute for Materials Science, 1-1 Namiki, Tsukuba 305-0044, Japan. [4]Materials Science and Technology Division, Oak Ridge National Laboratory, Oak Ridge, TN 37831, USA. [5]Department of Physics and Center of Theoretical and Computational Physics, University of Hong Kong, Hong Kong, China. [6]Department of Electrical Engineering, University of Washington, Seattle, WA 98195, USA. [7]Department of Materials Science and Engineering, University of Washington, Seattle, WA 98195, USA.
*These authors contributed equally to this work.
†Corresponding author. Email: xuxd@uw.edu

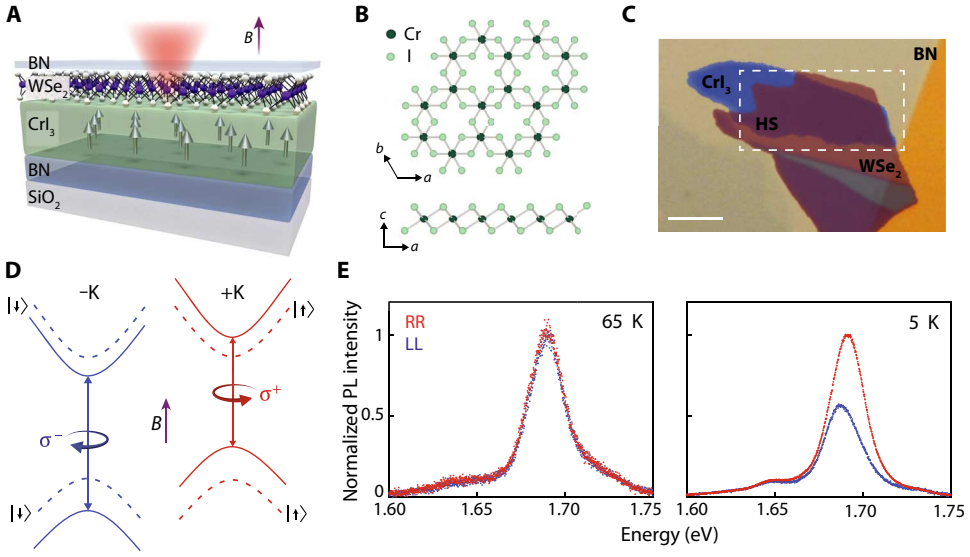

Fig. 1. Ultrathin CrI_3/WSe_2 heterostructure and observation of spontaneous magnetization. (**A**) Schematic of van der Waals heterostructure formed by monolayer WSe_2 and ferromagnetic-layered semiconductor CrI_3 and encapsulated by h-BN. (**B**) Top and side views of CrI_3 crystal structure. (**C**) Optical microscope image of device 2. The WSe_2/CrI_3 heterostructure is sandwiched by optically transparent h-BN. Scale bar, 5 μm. (**D**) Spin-valley locking effect and valley-dependent optical selection rules in monolayer WSe_2. Dashed (solid) lines indicate the band edges before (after) exchange field coupling. Black arrows denote spins. (**E**) Circularly polarized PL spectra above T_C (65 K, left) and below T_C (5 K, right) in the absence of an applied magnetic field. It is evident that the valley degeneracy is lifted at 5 K because of the magnetic proximity effect.

RESULTS

Observation of zero-field valley splitting and polarization

The sample is cooled in a helium cryostat and excited by a HeNe laser (1.96 eV). Below, we label the polarized photoluminescence (PL) spectra as P_1P_2, where P_1 (P_2) represents the excitation (detection) polarization, which can be either right (R, σ+) or left (L, σ−) circularly polarized. Figure 1E (left panel) displays a typical PL spectrum of device 1 at a temperature of 65 K, which is above the T_C of CrI_3. We attribute the PL to a positively charged trion state in WSe_2 due to the type II band alignment, with the CrI_3 conduction band lying below that of WSe_2 (sections S1 and S2). Here, the RR and LL spectra are nearly identical, as expected from time-reversal symmetry between the valleys in WSe_2.

Remarkably, the valley degeneracy is lifted as the sample is cooled below the T_C of CrI_3. Figure 1E (right panel) shows a representative spectrum taken at 5 K. The RR spectrum exhibits both a larger peak intensity and energy than LL. The extracted valley splitting between RR and LL spectra is about 3.5 meV (see section S3 for fitting details), equivalent to an effective magnetic field of about 13 T (section S4). Further measurements reveal that the magnitude of the valley splitting is independent of the excitation power (section S5), which rules out carrier density effects as a dominant mechanism for the valley splitting. Thus, we attribute the energy splitting to a strong magnetic exchange field between the CrI_3 spins and WSe_2 excitons. We emphasize that because the optical transition is determined by the energy difference between the conduction and valence bands, the observed valley splitting reflects the distinct coupling of the exchange field with the conduction and valence bands (Fig. 1D, solid lines). This is due to the different orbital character of the conduction and valence band edges (*19*, *20*).

Ferromagnetic substrate control of valley dynamics

We further study the polarized PL while sweeping an applied magnetic field **B** perpendicular to the sample plane (Faraday geometry, **B** parallel to easy axis; Fig. 1A). In Fig. 2A, the total PL intensity (I) for L excitation ($I_{LL} + I_{LR}$) and R excitation ($I_{RR} + I_{RL}$) is plotted as a function of applied magnetic field and emission energy for device 1. Six distinct regimes are denoted by the arrows, with three sharp jumps in PL intensity and peak energy near 0 and ±0.85 T and two smaller jumps near ±1.85 T. Figure 2B illustrates the overlaid RR and LL spectra at the six selected magnetic fields corresponding to each regime, highlighting the multiple jumps in peak energy and intensity. In Fig. 2 (C and D), we display the valley splitting and the normalized difference between RR and LL intensities, $\rho = \frac{I_{RR} - I_{LL}}{I_{RR} + I_{LL}}$, as a function of increasing (orange curve) and decreasing (green curve) applied magnetic field. Hysteresis loops, which are a hallmark of ferromagnetic effects, are observed at $B = \pm 0.85$ and 0 T. The widths of observed hysteresis loops are around 50 mT. Similar measurements in Voigt geometry (**B** parallel to the sample plane) demonstrate a rotation of the magnetization from in-plane to out-of-plane as the applied magnetic field is reduced to zero, confirming the out-of-plane easy axis in ultrathin CrI_3 (section S6). In the following discussions, we ignore the direct influence of the applied magnetic field on WSe_2 PL intensity and energy (*31*, *32*, *37*, *38*) because the exchange field is much stronger than the applied field (typically below ~1 T).

A notable observation in Fig. 2A is that at a fixed applied magnetic field, the total PL intensity strongly depends on the excitation helicity. To understand this phenomenon, we focus on the regime with $B > 0.9$ T, where the CrI_3 magnetization **M** is nearly aligned with **B.** As shown in Fig. 1D, R and L excitations create $|K, \uparrow\rangle$ and $|-K, \downarrow\rangle$ electrons, respectively, where ↑ (↓) represents the electron spin orientation. In CrI_3, the lowest-energy unoccupied conduction bands are mainly composed of the spin-polarized e_g orbitals of the Cr atom, with spin orientation parallel to the ground-state spin (section S1). Therefore, electron hopping from WSe_2 to CrI_3 is only allowed for the aligned spin $|K, \uparrow\rangle$ (Fig. 2E). Under the condition that optical absorption at 1.96 eV is independent of light helicity (section S7), the electron spins created by R excitation have an extra nonradiative relaxation channel compared to L excitation. This results in a strongly quenched PL as well as a broader spectral linewidth compared to L excitation. The helicity-dependent PL is similar to that observed recently in an epitaxially grown

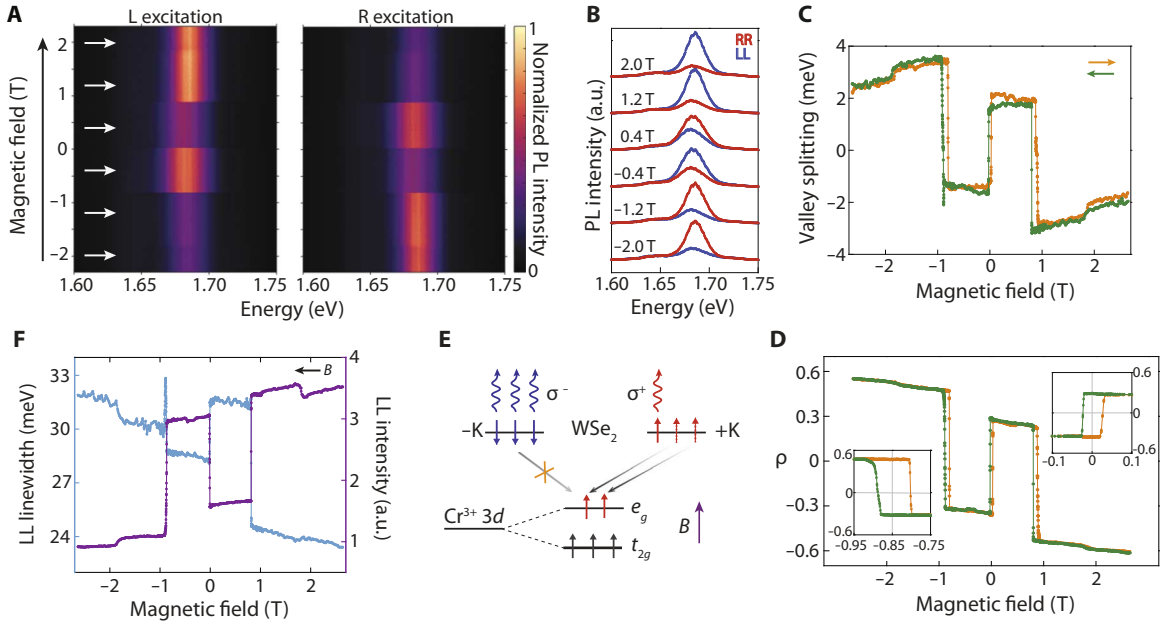

Fig. 2. Ferromagnetic substrate control of spin and valley pseudospin dynamics. (**A**) Maps of the total PL intensity as a function of emission energy and applied magnetic field for left circular (L) and right circular (R) excitation. The black arrow indicates the applied magnetic field sweeping direction. (**B**) RR and LL spectra at selected magnetic fields [indicated by the white arrows in (A)]. See text for definition of RR and LL. a.u., arbitrary units. (**C**) Valley splitting and (**D**) normalized PL intensity difference between RR and LL (ρ) as a function of applied magnetic field sweeping up (orange) and down (green). Insets in (D) are zoomed-in plots of hysteresis curves. (**E**) Schematic depicting the spin orientation–dependent charge hopping between WSe_2 and CrI_3, which leads to the excitation helicity-dependent PL intensity in (A). See text for detailed description. (**F**) PL spectral linewidth (blue) and intensity (purple) versus applied magnetic field (sweeping from positive to negative) for the LL condition. Broad width is always associated with weak PL intensity.

ferromagnet/quantum well heterostructure (*39*); however, the PL polarization and intensity modulation are an order of magnitude stronger in our system with an order-of-magnitude smaller applied magnetic field range (section S8).

In Fig. 2F, we plot the extracted linewidth and PL intensity of the LL spectrum versus applied magnetic field. The general trend is that the linewidth broadens whenever the PL intensity decreases, and vice versa. This is further evidence supporting the proposed physical picture that in the spin-aligned configuration, the allowed charge hopping opens up an additional nonradiative relaxation channel. We can estimate the hopping rate by the difference in spectral width between RR and LL conditions. For $B = 1$ T, the difference is ~5 meV, implying a spin-dependent charge hopping rate on the order of $\frac{\hbar}{5\,\mathrm{meV}} \approx 130$ fs where $\hbar$ is the reduced Planck constant. Moreover, the spectral widths vary with the applied magnetic field (section S9), suggesting that the hopping rate can be tuned by controlling the CrI_3 magnetization.

Another outstanding feature in Fig. 2 (C and D) is the sharp change of the valley splitting and ρ near $B = \pm 0.85$ and 0 T (movie S1). For example, when sweeping the applied magnetic field down through the transition near $B = -0.85$ T, the valley splitting changes from −1.3 to 3.4 meV in a span of about 30 mT (Fig. 2C). This corresponds to a valley splitting rate of over 150 meV/T, nearly three orders of magnitude larger than can be achieved by the Zeeman effect in bare WSe_2. Moreover, when sweeping through −0.8 T in the other direction and also near zero field, the switching is even faster, occurring within a span of ≤6 mT (section S10). We also note that the critical fields are independent of the sweep rate (section S11). The sign change of the valley splitting and ρ implies a flip of the CrI_3 magnetization. This behavior is expected for a ferromagnet when the applied magnetic field crosses zero. However, the sign change near ±0.85 T is intriguing because the field has not changed direction. This complicated magnetic field dependence implies rich magnetization dynamics in the ultrathin CrI_3 substrate. By comparison, bulk CrI_3 exhibits the expected magnetization loop at zero magnetic field with small remanence and coercivity (*36*).

PL imaging of magnetic domain dynamics

Because both the valley splitting and ρ are tightly connected to the CrI_3 magnetization, spatial maps of these parameters should reveal the underlying magnetic domain structure. Inspired by this idea, we performed spatially resolved, polarized PL measurements as a function of applied magnetic field on device 2 (boxed region in Fig. 1C). Figure 3 displays spatial maps of ρ as a function of magnetic field sweeping direction, which are ordered to highlight time-reversal pairs (see section S12 for valley splitting maps). The time-reversal pair consists of two maps acquired at opposite applied magnetic fields while sweeping in the opposite direction. We find that each time-reversal pair shows excellent consistency in their pattern except for the opposite sign, validating the stability of the system. The domain structure and ρ disappear above ~60 K (section S13), indicating that T_C is similar to bulk CrI_3 (*36*).

These maps reveal the evolution of the domain structure between −1.1 and 1.1 T in ultrathin CrI_3. When the applied magnetic field is larger than the coercive field, the uniform color across the entire heterostructure indicates full magnetization of CrI_3. When the applied magnetic field is set at an intermediate value, a multidomain structure appears with a domain size on the order of a few micrometers. We define domains that only switch signs with the reversal of the applied field as strong domains (indicated by the red arrow in the $B = -0.5$ T map) while those that flip without switching the applied field as weak domains (indicated by the blue arrow). Unlike the strong domains, the

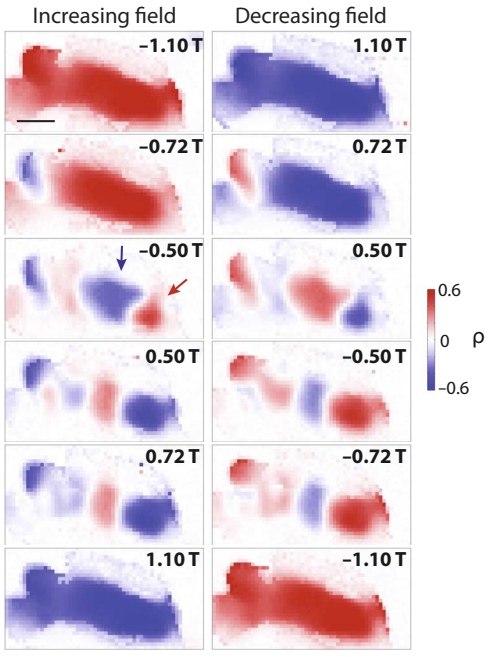

Fig. 3. Polarization-resolved micro-PL imaging of domain structures. Each panel is a spatial map of ρ (see text for definition) at the indicated applied magnetic field. Left and right columns are arranged in a time-reversal manner corresponding to increasing (left) and decreasing (right) applied magnetic field, respectively. The blue arrow indicates a domain in which the sign of ρ flips three times by sweeping the field, whereas the red arrow points to a domain that flips the sign of ρ only once. Scale bar, 3 μm.

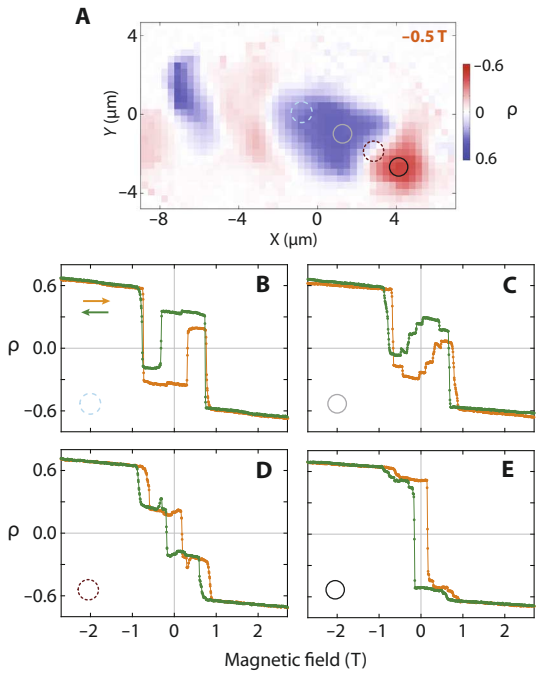

Fig. 4. Position-sensitive ferromagnetic domain dynamics. (**A**) Spatial map of ρ from Fig. 3 (−0.5 T, sweep down) with blue, gray, brown, and black circles indicating the spots of selected magnetic field sweeps of ρ in (**B**), (**C**), (**D**), and (**E**).

weak domains flip three times within one sweep. Therefore, if the laser spot is on a weak domain, the corresponding valley splitting and ρ will also flip three times within one sweep, which is consistent with the observation in Fig. 2 (C and D). A plausible interpretation of the multiple flips is the competition between the Zeeman energy and the magnetic dipole energy between strong and weak domains. In a certain applied magnetic field range, the dipolar interaction exceeds the Zeeman energy in a weak domain, which causes it to flip to reduce the magnetic dipole energy. A simple model of the magnetic domain evolution, which considers the Zeeman energy, the dipolar interaction between strong and weak domains, and the easy-axis anisotropy, qualitatively reproduces the observed curves in Fig. 2C (section S14).

DISCUSSION

Measurement of the valley-polarized exciton PL in WSe_2 additionally provides a new local probe to investigate spin and domain dynamics in adjacent ferromagnets through van der Waals engineering. Figure 4 shows multiple distinct ρ-*B* curves at different sample positions. As expected from the spatial maps in Fig. 3, if the laser is focused on a weak domain (Fig. 4, B and C), the magnetization can flip without changing the applied magnetic field direction, whereas in a strong domain (Fig. 4E), there is only one hysteresis loop centered at zero field. In addition to coarse changes in magnetization, fine structure is also observed. For instance, in Fig. 4C, we observe fine steps of ρ as the applied magnetic field varies. At first glance, the observation is an echo of the Barkhausen effect due to the rapid change of the domain size in ferromagnets. However, the laser spot is toward the center of the weak domain, which is less likely to be affected by changes in domain size. Furthermore, the ρ-*B* curves near the domain boundary do not exhibit these fine steps, as seen in Fig. 4D. One possibility to consider is whether the magnetization in thin CrI_3 can flip layer by layer, as in certain types of layered antiferromagnets (*40*, *41*). Detailed CrI_3 thickness dependence will be crucial to help understand the electronic and magnetic coupling beyond the heterostructure interface. In addition, Fig. 4D displays an overshoot of ρ (or spikes) that may be related to negative differential magnetization (*42*). Further interesting topics include unraveling the origin of the slow jumps at ±1.85T, which manifest themselves as an opposite trend in Fig. 2 (C and D), and may indicate a different origin from the other jumps at lower fields.

These intriguing phenomena will require additional study to elucidate the underlying mechanisms. However, it is already evident that this probe is highly sensitive to spin interactions and magnetization dynamics, providing a powerful addition to conventional techniques such as magneto-optical Kerr rotation in studying magnetism in thin films. In addition, the integration of van der Waals magnetic materials into other heterostructures should empower researchers to harness exchange interactions and interfacial effects to explore novel physical phenomena and spintronics at the atomically thin limit.

MATERIALS AND METHODS

Device fabrication

Bulk crystals of WSe_2, CrI_3, and h-BN were first exfoliated onto a 90-nm SiO_2 on Si. Because of the instability of CrI_3 in air, we performed exfoliation in a glove box with O_2 and H_2O levels below 0.5 parts per million. Immediately after finding the CrI_3 sample, we assembled the heterostructure stack (h-BN/CrI_3/monolayer WSe_2/h-BN) using a polycarbonate-based transfer technique (*43*) in a glove box. The h-BN thickness was about 20 nm, and CrI_3 thickness was ~10 nm. The chloroform rinse was performed in ambient environment for 2 min. We note that bare CrI_3 flakes readily hydrate in air, decomposing within seconds. There were

no signs of degradation in the h-BN–sandwiched sample under ambient conditions for at least an hour, allowing us to transport and mount the sample for measurement.

Photoluminescence

The samples were measured in a continuous helium flow cryostat with a 7-T superconducting magnet, which can operate in both Faraday and Voigt geometry. PL measurements were performed in reflection geometry using continuous-wave excitation from a HeNe laser (1.96 eV) that was power-stabilized (30 μW) and focused to ~1 μm with an aspheric lens. The back-reflected PL was collected by the same lens and detected using a spectrometer and Si charge-coupled device. Samples were measured at 5 K and in Faraday geometry, unless otherwise specified. For the magnetic field–dependent measurements, we continuously scanned the magnetic field and collected a full hysteresis sweep (up and down in applied magnetic field) for each polarization configuration before switching to the next polarization. Good overlap at saturation magnetic fields indicated the stability of the measurement and allowed comparison of magnetic field–dependent data between different polarizations.

A two-axis piezoelectric scanning mirror was used to scan the laser spot over the sample for spatially resolved measurements. Liquid-crystal variable wave plates were used to allow repeatable and quick (<100 ms) switching between different circular polarizations for excitation and collection. Thus, we took both RR and LL polarization configurations at each pixel (1-s integration for each polarization) before moving the laser, which rules out sample drift effects in our data. As shown in Fig. 3, there is an evident time-reversal symmetry between R and L polarized excitation versus applied magnetic fields. For magnetic field–dependent data at selected sample positions in Fig. 4, we simply took RR data and time-reversed it to obtain expected LL data and then compared them to determine the expected ρ.

SUPPLEMENTARY MATERIALS

Supplementary material for this article is available at http://advances.sciencemag.org/cgi/content/full/3/5/e1603113/DC1

section S1. Electronic structure of CrI_3/WSe_2 bilayer
section S2. Linear polarization
section S3. Peak parameter extraction
section S4. Comparison of valley splitting between bare WSe_2 and WSe_2/CrI_3
section S5. Power dependence of valley splitting
section S6. Voigt geometry
section S7. Helicity-independent differential reflection at the excitation energy
section S8. Valley polarization and intensity modulation parameter
section S9. Linewidth difference between polarizations
section S10. Rapid switching of heterostructure PL
section S11. Magnetic field sweep rate dependence
section S12. Spatial maps of valley splitting
section S13. Temperature dependence
section S14. Model of strong and weak domains
movie S1. Circularly polarized PL in a changing external magnetic field.
fig. S1. The atomic structure and the electronic band structure of the CrI_3-WSe_2 bilayer.
fig. S2. Linearly polarized excitation and detection.
fig. S3. Peak parameter extraction.
fig. S4. Valley splitting in bare WSe_2 and WSe_2/CrI_3.
fig. S5. Power dependence of valley splitting.
fig. S6. PL measurements in Voigt geometry.
fig. S7. Differential reflection spectrum of WSe_2/CrI_3.
fig. S8. Valley polarization and intensity modulation parameter.
fig. S9. Linewidth difference between polarizations.
fig. S10. Rapid switching of PL in WSe_2/CrI_3.
fig. S11. Sweep rate dependence.
fig. S12. Spatial maps of valley splitting.
fig. S13. Temperature dependence of CrI_3 magnetization.
fig. S14. Strong- and weak-domain modeling.
table S1. The free energy and its second-order derivatives with respect to the angles of the two domains.
References (*44*–*50*)

REFERENCES AND NOTES

1. M. D. Stiles, Interlayer exchange coupling. *J. Magn. Magn. Mater.* **200**, 322–337 (1999).
2. M. N. Baibich, J. M. Broto, A. Fert, F. Nguyen Van Dau, F. Petroff, P. Etienne, G. Creuzet, A. Friederich, J. Chazelas, Giant magnetoresistance of (001)Fe/(001)Cr magnetic superlattices. *Phys. Rev. Lett.* **61**, 2472–2475 (1988).
3. G. Binasch, P. Grünberg, F. Saurenbach, W. Zinn, Enhanced magnetoresistance in layered magnetic structures with antiferromagnetic interlayer exchange. *Phys. Rev. B* **39**, 4828–4830 (1989).
4. A. E. Berkowitz, K. Takano, Exchange anisotropy—A review. *J. Magn. Magn. Mater.* **200**, 552–570 (1999).
5. J.-G. Zhu, C. Park, Magnetic tunnel junctions. *Mater. Today* **9**, 36–45 (2006).
6. A. I. Buzdin, Proximity effects in superconductor-ferromagnet heterostructures. *Rev. Mod. Phys.* **77**, 935–976 (2005).
7. C. Lee, F. Katmis, P. Jarillo-Herrero, J. S. Moodera, N. Gedik, Direct measurement of proximity-induced magnetism at the interface between a topological insulator and a ferromagnet. *Nat. Commun.* **7**, 12014 (2016).
8. F. Katmis, V. Lauter, F. S. Nogueira, B. A. Assaf, M. E. Jamer, P. Wei, B. Satpati, J. W. Freeland, I. Eremin, D. Heiman, P. Jarillo-Herrero, J. S. Moodera, A high-temperature ferromagnetic topological insulating phase by proximity coupling. *Nature* **533**, 513–516 (2016).
9. A. H. MacDonald, P. Schiffer, N. Samarth, Ferromagnetic semiconductors: Moving beyond (Ga,Mn)As. *Nat. Mater.* **4**, 195–202 (2005).
10. J. Fabian, C. Matos-Abiague, P. Ertler, I. Stano, I. Zutic, Semiconductor spintronics. *Acta Phys. Slovaca* **57**, 565 (2007).
11. G. A. Prinz, Hybrid ferromagnetic-semiconductor structure. *Science* **250**, 1092–1097 (1990).
12. R. I. Dzhioev, B. P. Zakharchenya, P. A. Ivanov, V. L. Korenov, Detection of the magnetization of a ferromagnetic film in a Ni/GaAs structure from the polarization of electrons of the semiconductor. *JETP Lett.* **60**, 650–654 (1994).
13. V. L. Korenev, M. Salewski, I. A. Akimov, V. F. Sapega, L. Langer, I. V. Kalitukha, J. Debus, R. I. Dzhioev, D. R. Yakovlev, D. Müller, C. Schröder, H. Hövel, G. Karczewski, M. Wiater, T. Wojtowicz, Y. G. Kusrayev, M. Bayer, Long-range *p*–*d* exchange interaction in a ferromagnet–semiconductor hybrid structure. *Nat. Phys.* **12**, 85–91 (2016).
14. R. C. Myers, A. C. Gossard, D. D. Awschalom, Tunable spin polarization in III-V quantum wells with a ferromagnetic barrier. *Phys. Rev. B* **69**, 161305 (2004).
15. H. X. Yang, A. Hallal, D. Terrade, X. Waintal, S. Roche, M. Chshiev, Proximity effects induced in graphene by magnetic insulators: First-principles calculations on spin filtering and exchange-splitting gaps. *Phys. Rev. Lett.* **110**, 46603 (2013).
16. H. Haugen, D. Huertas-Hernando, A. Brataas, Spin transport in proximity-induced ferromagnetic graphene. *Phys. Rev. B* **77**, 115406 (2008).
17. Z. Qiao, S. A. Yang, W. Feng, W.-K. Tse, J. Ding, Y. Yao, J. Wang, Q. Niu, Quantum anomalous Hall effect in graphene from Rashba and exchange effects. *Phys. Rev. B* **82**, 161414 (2010).
18. Z. Qiao, W. Ren, H. Chen, L. Bellaiche, Z. Zhang, A. H. MacDonald, Q. Niu, Quantum anomalous Hall effect in graphene proximity coupled to an antiferromagnetic insulator. *Phys. Rev. Lett.* **112**, 116404 (2014).
19. J. Qi, X. Li, Q. Niu, J. Feng, Giant and tunable valley degeneracy splitting in $MoTe_2$. *Phys. Rev. B* **92**, 121403 (2015).
20. Q. Zhang, S. A. Yang, W. Mi, Y. Cheng, U. Schwingenschlögl, Large spin-valley polarization in monolayer $MoTe_2$ on top of EuO(111). *Adv. Mater.* **28**, 959–966 (2016).
21. W. Han, R. K. Kawakami, M. Gmitra, J. Fabian, Graphene spintronics. *Nat. Nanotechnol.* **9**, 794–807 (2014).
22. P. Wei, S. Lee, F. Lemaitre, L. Pinel, D. Cutaia, W. Cha, F. Katmis, Y. Zhu, D. Heiman, J. Hone, J. S. Moodera, C.-T. Chen, Strong interfacial exchange field in the graphene/EuS heterostructure. *Nat. Mater.* **15**, 711–716 (2016).
23. Z. Wang, C. Tang, R. Sachs, Y. Barlas, J. Shi, Proximity-induced ferromagnetism in graphene revealed by the anomalous Hall effect. *Phys. Rev. Lett.* **114**, 016603 (2015).
24. O. L. Sanchez, D. Ovchinnikov, S. Misra, A. Allain, A. Kis, Valley polarization by spin injection in a light-emitting van der Waals heterojunction. *Nano Lett.* **16**, 5792–5797 (2016).
25. Y. Ye, J. Xiao, H. Wang, Z. Ye, H. Zhu, M. Zhao, Y. Wang, J. Zhao, X. Yin, X. Zhang, Electrical generation and control of the valley carriers in a monolayer transition metal dichalcogenide. *Nat. Nanotechnol.* **11**, 598–602 (2016).
26. A. K. Geim, I. V. Grigorieva, Van der Waals heterostructures. *Nature* **499**, 419–425 (2013).
27. K. S. Novoselov, A. Mishchenko, A. Carvalho, A. H. C. Neto, O. Road, 2D materials and van der Waals heterostructures. *Science* **353**, aac9439 (2016).

28. J. Zhang, B. Zhao, Y. Yao, Z. Yang, Robust quantum anomalous Hall effect in graphene-based van der Waals heterostructures. *Phys. Rev. B* **92**, 165418 (2015).
29. D. Xiao, G.-B. Liu, W. Feng, X. Xu, W. Yao, Coupled spin and valley physics in monolayers of MoS_2 and other group-VI dichalcogenides. *Phys. Rev. Lett.* **108**, 196802 (2012).
30. X. Xu, W. Yao, D. Xiao, T. F. Heinz, Spin and pseudospins in layered transition metal dichalcogenides. *Nat. Phys.* **10**, 343–350 (2014).
31. G. Aivazian, Z. Gong, A. M. Jones, R.-L. Chu, J. Yan, D. G. Mandrus, C. Zhang, D. Cobden, W. Yao, X. Xu, Magnetic control of valley pseudospin in monolayer WSe_2. *Nat. Phys.* **11**, 148–152 (2015).
32. A. Srivastava, M. Sidler, A. V. Allain, D. S. Lembke, A. Kis, A. Imamoğlu, Valley Zeeman effect in elementary optical excitations of monolayer WSe_2. *Nat. Phys.* **11**, 141–147 (2015).
33. D. MacNeill, C. Heikes, K. F. Mak, Z. Anderson, A. Kormányos, V. Zólyomi, J. Park, D. C. Ralph, Breaking of valley degeneracy by magnetic field in monolayer $MoSe_2$. *Phys. Rev. Lett.* **114**, 037401 (2015).
34. Y. Li, J. Ludwig, T. Low, A. Chernikov, X. Cui, G. Arefe, Y. D. Kim, A. M. van der Zande, A. Rigosi, H. M. Hill, S. H. Kim, J. Hone, Z. Li, D. Smirnov, T. F. Heinz, Valley splitting and polarization by the Zeeman effect in monolayer $MoSe_2$. *Phys. Rev. Lett.* **113**, 266804 (2014).
35. J. F. Dillon Jr., H. Kamimura, J. P. Remeika, Magneto-optical properties of ferromagnetic chromium trihalides. *J. Phys. Chem. Solids* **27**, 1531–1549 (1966).
36. M. A. McGuire, H. Dixit, V. R. Cooper, B. C. Sales, Coupling of crystal structure and magnetism in the layered, ferromagnetic insulator CrI_3. *Chem. Mater.* **27**, 612–620 (2015).
37. G. Wang, L. Bouet, M. M. Glazov, T. Amand, E. L. Ivchenko, E. Palleau, X. Marie, B. Urbaszek, Magneto-optics in transition metal diselenide monolayers. *2D Mater.* **2**, 34002 (2015).
38. A. A. Mitioglu, P. Plochocka, Á. Granados del Aguila, P. C. M. Christianen, G. Deligeorgis, S. Anghel, L. Kulyuk, D. K. Maude, Optical investigation of monolayer and bulk tungsten diselenide (WSe_2) in high magnetic fields. *Nano Lett.* **15**, 4387–4392 (2015).
39. V. L. Korenev, I. A. Akimov, S. V. Zaitsev, V. F. Sapega, L. Langer, D. R. Yakovlev, Y. A. Danilov, M. Bayer, Dynamic spin polarization by orientation-dependent separation in a ferromagnet–semiconductor hybrid. *Nat. Commun.* **3**, 959 (2012).
40. O. Hellwig, T. L. Kirk, J. B. Kortright, A. Berger, E. E. Fullerton, A new phase diagram for layered antiferromagnetic films. *Nat. Mater.* **2**, 112–116 (2003).
41. O. Hellwig, A. Berger, E. E. Fullerton, Domain walls in antiferromagnetically coupled multilayer films. *Phys. Rev. Lett.* **91**, 197203 (2003).
42. Y. Yao, H. C. Mireles, J. Liu, Q. Niu, J. L. Erskine, Negative differential magnetization in ultrathin Fe on vicinal W(100). *Phys. Rev. B* **67**, 174409 (2003).
43. P. J. Zomer, M. H. D. Guimarães, J. C. Brant, N. Tombros, B. J. van Wees, Fast pick up technique for high quality heterostructures of bilayer graphene and hexagonal boron nitride. *Appl. Phys. Lett.* **105**, 013101 (2014).
44. J. P. Perdew, K. Burke, M. Ernzerhof, Generalized gradient approximation made simple. *Phys. Rev. Lett.* **77**, 3865–3868 (1996).
45. J. P. Perdew, K. Burke, M. Ernzerhof, Generalized gradient approximation made simple. *Phys. Rev. Lett.* **78**, 1396 (1997).
46. P. Giannozzi, S. Baroni, N. Bonini, M. Calandra, R. Car, C. Cavazzoni, D. Ceresoli, G. L. Chiarotti, M. Cococcioni, I. Dabo, A. Dal Corso, S. de Gironcoli, S. Fabris, G. Fratesi, R. Gebauer, U. Gerstmann, C. Gougoussis, A. Kokalj, M. Lazzeri, L. Martin-Samos, N. Marzari, F. Mauri, R. Mazzarello, S. Paolini, A. Pasquarello, L. Paulatto, C. Sbraccia, S. Scandolo, G. Sclauzero, A. P. Seitsonen, A. Smogunov, P. Umari, R. M. Wentzcovitch, QUANTUM ESPRESSO: A modular and open-source software project for quantum simulations of materials. *J. Phys. Condens. Matter* **21**, 395502 (2009).
47. S. Grimme, Semiempirical GGA-type density functional constructed with a long-range dispersion correction. *J. Comput. Chem.* **27**, 1787–1799 (2006).
48. V. Barone, M. Casarin, D. Forrer, M. Pavone, M. Sambi, A. Vittadini, Role and effective treatment of dispersive forces in materials: Polyethylene and graphite crystals as test cases. *J. Comput. Chem.* **30**, 934–939 (2009).
49. A. M. Jones, H. Yu, N. J. Ghimire, S. Wu, G. Aivazian, J. S. Ross, B. Zhao, J. Yan, D. G. Mandrus, D. Xiao, W. Yao, X. Xu, Optical generation of excitonic valley coherence in monolayer WSe_2. *Nat. Nanotechnol.* **8**, 634–638 (2013).
50. S. Esho, Anomalous magneto-optical hysteresis loops of sputtered Gd-Co films. *Jpn. J. Appl. Phys.* **15**, 93–98 (1976).

Acknowledgments

Funding: This work was mainly supported by the U.S. Department of Energy, Basic Energy Sciences, Materials Sciences and Engineering Division (DE-SC0008145 and SC0012509) and University of Washington Innovation Award. W.Y. was supported by the Croucher Foundation (Croucher Innovation Award), the Research Grants Council of Hong Kong (HKU17305914P), and the Hong Kong University Outstanding Researcher Award. Work at Oak Ridge National Laboratory (M.A.M.) was supported by the U.S. Department of Energy, Office of Science, Basic Energy Sciences, Materials Sciences and Engineering Division. K.W. and T.T. acknowledge support from the Elemental Strategy Initiative conducted by the Ministry of Education, Culture, Sports, Science and Technology, Japan and a Grant-in-Aid for Scientific Research on Innovative Areas "Science of Atomic Layers" from the Japan Society for the Promotion of Science. X.X., D.X., and K.-M.C.F. acknowledge the support from the Cottrell Scholar Award. X.X. acknowledges the support from the State of Washington–funded Clean Energy Institute and from the Boeing Distinguished Professorship in Physics. **Author contributions:** X.X. conceived the project. D.Z. and B.H. fabricated the sample. K.L.S., D.Z., and X.L. performed the experiment, which is assisted by E.S. and supervised by X.X. and K.-M.C.F. M.A.M. synthesized and characterized the bulk CrI_3 crystal. T.T. and K.W. synthesized and characterized the bulk BN crystal. R.C., N.S., D.X., and W.Y. provided the theoretical support. X.X., K.L.S., D.Z., and D.X. wrote the paper with input from all authors. All authors discussed the results. **Competing interests:** The authors declare that they have no competing interests. **Data and materials availability:** All data needed to evaluate the conclusions in the paper are present in the paper and/or the Supplementary Materials. Additional data related to this paper may be requested from the authors.

Submitted 7 December 2016
Accepted 3 April 2017
Published 31 May 2017
10.1126/sciadv.1603113

Citation: D. Zhong, K. L. Seyler, X. Linpeng, R. Cheng, N. Sivadas, B. Huang, E. Schmidgall, T. Taniguchi, K. Watanabe, M. A. McGuire, W. Yao, D. Xiao, K.-M. C. Fu, X. Xu, Van der Waals engineering of ferromagnetic semiconductor heterostructures for spin and valleytronics. *Sci. Adv.* **3**, e1603113 (2017).